RESEARCH ARTICLE

NANOMATERIALS

Reductive pathways in molten inorganic salts enable colloidal synthesis of III-V semiconductor nanocrystals

Justin C. Ondry[1], Zirui Zhou[1], Kailai Lin[2,3], Aritrajit Gupta[1], Jun Hyuk Chang[1], Haoqi Wu[1], Ahhyun Jeong[1], Benjamin F. Hammel[4], Di Wang[1], H. Christopher Fry[5], Sadegh Yazdi[4,6], Gordana Dukovic[4,6,7], Richard D. Schaller[5,8], Eran Rabani[2,3,9], Dmitri V. Talapin[1,5,10]*

Colloidal quantum dots, with their size-tunable optoelectronic properties and scalable synthesis, enable applications in which inexpensive high-performance semiconductors are needed. Synthesis science breakthroughs have been key to the realization of quantum dot technologies, but important group III–group V semiconductors, including colloidal gallium arsenide (GaAs), still cannot be synthesized with existing approaches. The high-temperature molten salt colloidal synthesis introduced in this work enables the preparation of previously intractable colloidal materials. We directly nucleated and grew colloidal quantum dots in molten inorganic salts by harnessing molten salt redox chemistry and using surfactant additives for nanocrystal shape control. Synthesis temperatures above 425°C are critical for realizing photoluminescent GaAs quantum dots, which emphasizes the importance of high temperatures enabled by molten salt solvents. We generalize the methodology and demonstrate nearly a dozen III-V solid-solution nanocrystal compositions that have not been previously reported.

Nanometer-size crystals of semiconductor materials demonstrate size-dependent physical and chemical properties that can be exploited in displays, lasers, photodetectors, and solar cells (*1*). These materials also show promise for emerging applications in quantum information science (*2*), high-performance photonics (*3*), and photocatalysis (*4*). Successful commercial applications of quantum dots have proven that colloidal synthesis, which is inherently scalable, is competitive in terms of material quality with much more expensive semiconductor wafer and thin-film technologies such as molecular beam epitaxy (MBE) and chemical vapor deposition (CVD) (*5*). To date, nearly perfect control over size, shape, and physical properties has been achieved for colloidally synthesized II-VI semiconductors (zinc, cadmium, and mercury chalcogenides) (*6*–*8*), IV-VI semiconductors (lead chalcogenides) (*9*), lead halide perovskites (*10*), indium pnictides [indium phosphide (InP), indium arsenide (InAs), and indium antimonide (InSb)] (*11*–*16*), and other materials beyond semiconductors (*17*–*19*). However, there are still critical omissions for colloidal semiconductors. For example, the most efficient solar cells, brightest light-emitting diodes, most powerful semiconductor lasers, and fastest electronic devices use gallium pnictides such as gallium arsenide (GaAs), gallium nitride (GaN), and gallium-containing ternary and quaternary III-V materials (*20*). Numerous attempts to synthesize colloidal gallium pnictides with solution methods have only produced defective materials with no band-edge emission (*21*–*23*).

High temperature is beneficial for growing defect-free crystals, and colloidal nanocrystals (NCs) are often synthesized at the highest temperatures that can be tolerated by the organic solvents and surfactants used (*3*, *6*). This set of observations, compounded with knowledge of the poor quality of GaAs grown by means of low-temperature MBE (*24*, *25*), suggests that the colloidal synthesis of gallium pnictide NCs may require temperatures that are incompatible with any organic solvent. Furthermore, the much higher Lewis acidity of molecular Ga^{III} species compared with In^{III} or Cd^{II} species promotes side reactions of gallium precursors with organic molecules.

Molten inorganic salts can provide much greater thermal stability, improved chemical stability, and wider electrochemical windows as compared with those of organic solvents (*26*–*28*). Recent demonstrations of the colloidal stability of NCs in molten inorganic salts (*29*, *30*) inspired our exploration of molten salts for colloidal synthesis. We have demonstrated that colloidal InP and InAs NCs presynthesized in organic solvents can be converted through partial cation exchange into $In_{1-x}Ga_xP$ and $In_{1-x}Ga_xAs$ NCs by annealing them in gallium-containing molten salts at temperatures from 350° to 500°C (*31*–*33*). The resulting $In_{1-x}Ga_xP$ and $In_{1-x}Ga_xAs$ NCs show strong photoluminescence (PL) and other desirable photophysical properties, thus proving the potential of molten salts as solvents for the synthesis of previously inaccessible colloidal III-V semiconductors (*33*).

This work uncovers previously unknown dimensions for colloidal chemistry in molten salts. First, we elucidated the rich redox chemistry of molten salt solvents and demonstrated how control of redox processes can stabilize III-V NCs against decomposition. Next, we used new redox chemistry to nucleate and grow monodisperse colloidal GaAs, gallium phosphide (GaP), $GaP_{1-y}As_y$, and $GaAs_{1-y}Sb_y$ NCs directly in molten salts and demonstrated shape control using molten salt "surfactant" additives. Last, we demonstrated size-dependent band-edge PL for colloidal GaAs quantum dots.

Redox reactions of NCs in molten salts

Molten salt solvents can be classified by using the Lewis acid-base concept, in which group III halides such as GaX_3 (X = Cl, Br, or I) are Lewis acids; alkali halides such as potassium iodide (KI) are Lewis bases; and alkali halometallates such as $KGaI_4$, produced by the stoichiometric reaction of GaI_3 and KI, are Lewis-neutral. We have noticed that cation exchange reactions of III-V NCs in molten salts are particularly sensitive to the nature of the group V element. For example, InP could efficiently convert into $In_{1-x}Ga_xP$ in Lewis acidic (*34*), basic (*35*), or neutral molten salts, whereas the use of a Lewis-neutral $KGaI_4$ molten salt is key for preserving the chemical stability of InAs NCs and forming $In_{1-x}Ga_xAs$ phases (*32*). In addition, InSb always decomposes when a Ga^{III} source is added to molten salts in an attempt to synthesize $In_{1-x}Ga_xSb$ NCs.

InAs NCs underwent the following reaction in $KGaI_4$ molten salt: $InAs(c) + xKGaI_4(l) \rightarrow In_{1-x}Ga_xAs(c) + xKInI_4(l)$, where *c* and *l* stand for "colloidal" and "liquid," respectively. The $In_{1-x}Ga_xAs$ product could be identified with powder x-ray diffraction (XRD) (Fig. 1A), and $[InI_4]^-$ ions were detected with Raman spectroscopy (Fig. 1B). To understand the stability problem of antimonides in molten salts, we annealed InSb NCs in molten $KGaI_4$ (figs. S1 and S2 and materials and methods) and found no crystalline III-V products (Fig. 1C and fig. S3). Instead, the observation of Sb^0 by means of XRD suggested that Sb^{-III} in InSb was oxidized to Sb^0, which demonstrates the redox lability of the pnictide component of III-V NCs. Raman spectroscopy showed the formation of $[Ga_2I_6]^{2-}$ ions in the molten salt after the reaction (Fig. 1B and fig. S4). These Ga^{II}-containing ions indicate that $KGa^{III}I_4$ is being

[1]Department of Chemistry and James Franck Institute, University of Chicago, Chicago, IL 60637, USA. [2]Department of Chemistry, University of California, Berkeley, CA 94720, USA. [3]Materials Sciences Division, Lawrence Berkeley National Laboratory, Berkeley, CA 94720, USA. [4]Materials Science and Engineering, University of Colorado, Boulder, CO 80309, USA. [5]Center for Nanoscale Materials, Argonne National Laboratory, Argonne, IL 60439, USA. [6]Renewable and Sustainable Energy Institute, University of Colorado, Boulder, CO 80309, USA. [7]Department of Chemistry, University of Colorado, Boulder, CO 80309, USA. [8]Department of Chemistry, Northwestern University, Evanston, IL 60208, USA. [9]The Raymond and Beverly Sackler Center of Computational Molecular and Materials Science, Tel Aviv University, Tel Aviv 69978, Israel. [10]Pritzker School of Molecular Engineering, University of Chicago, Chicago, IL 60637, USA.
*Corresponding author. Email: dvtalapin@uchicago.edu

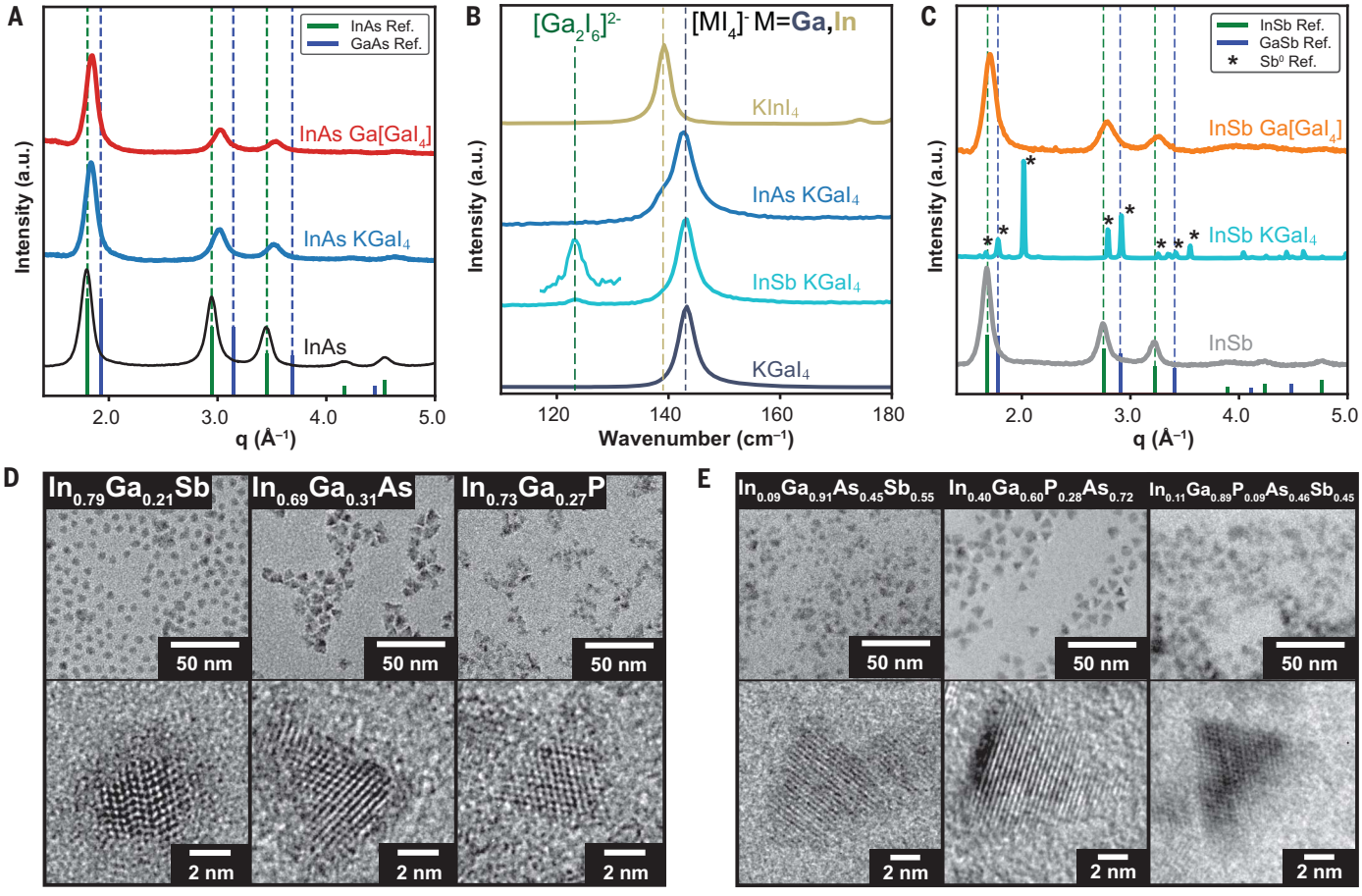

Fig. 1. Importance of redox potential control in molten salt solvents for transformation of III-V NCs. (**A**) Powder XRD patterns for (bottom) InAs NCs treated with (middle) $KGaI_4$ molten salt and (top) $Ga[GaI_4]$ molten salt at 400°C for 1 hour. a.u., arbitrary units. (**B**) Raman spectra of (bottom) $KGaI_4$ and (top) $KInI_4$ compared with spectra from the salt matrix after heating InSb NCs (light blue) and InAs NCs (dark blue), respectively, in $KGaI_4$. (**C**) Powder XRD patterns for (bottom) InSb NCs treated with (middle) $KGaI_4$ molten salt and (top) $Ga[GaI_4]$ molten salt at 325°C for 1 hour. (**D**) (Top) TEM and (bottom) HR-TEM images of $In_{1-x}Ga_xSb$, $In_{1-x}Ga_xAs$, and $In_{1-x}Ga_xP$ NCs with indicated compositions prepared by using $Ga[GaI_4]$. (**E**) (Top) TEM and (bottom) HR-TEM images of quaternary $In_{1-x}Ga_xAs_{1-y}Sb_y$ and pentanary $In_{1-x}Ga_xP_{1-y-z}As_ySb_z$ NCs with indicated compositions prepared by using $Ga[GaI_4]$ molten salt.

reduced by the InSb NCs in the following reaction: $In^{III}Sb^{-III}(c) + 2KGa^{III}I_4(l) \rightarrow Sb^0(s) + (K^+, In^+)_2[Ga^{II}{}_2I_6]^{2-}(l)$, where *s* stands for "solid."

Gallium (III) and indium (III) are the most common oxidation states of these elements, but molten halide salts can adopt a variety of compositions (supplementary text 1) that contain Ga^I, Ga^{II}, In^I, and In^{II} species (*36*). In a molten salt, the pnictide can act as a reducing agent for $KM^{III}X_4$ (where M is In or Ga), which leads to decomposition of the III-V NCs as schematically described in Fig. 2A. However, an analysis of redox equilibria suggests that the oxidation of Sb^{-III} to Sb^0 could be prevented if instead of Ga^{III} we used a molten salt with a weaker oxidizing potential. Annealing InSb NCs in molten $Ga^I[Ga^{III}I_4]$ (often referred to as Ga_2I_4) (supplementary text 1) at 325°C prevented oxidative decomposition of the antimonide (Fig. 1C). After annealing in $Ga[GaI_4]$, the XRD peaks from the InSb NCs shift to larger scattering vector *q* values ($q = 2\pi/d$, where *d* is the distance between the atomic planes), which indicates a decrease in lattice constant consistent with incorporation of gallium into the InSb lattice. By tuning the reaction time and temperature, we could synthesize $In_{1-x}Ga_xSb$ NCs from $x = 0$ to $x = 1$ (fig. S5).

Transmission electron microscopy (TEM) images of $In_{1-x}Ga_xSb$ NCs resulting from cation exchange of InSb NCs with $Ga[GaI_4]$ (Fig. 1D) showed well-separated NCs with a narrow size distribution and well-defined spherical shapes, which small-angle x-ray scattering (SAXS) corroborates (fig. S6). Similarly, $In_{1-x}Ga_xAs$ and $In_{1-x}Ga_xP$ NCs could be prepared from InAs and InP NCs by using molten $Ga[GaI_4]$ (Fig. 1, A and D, and fig. S7). We further expanded this reaction methodology to prepare quaternary and pentanary III-V colloidal NCs by reacting $InAs_{1-y}Sb_y$, $InP_{1-y}As_y$, $InP_{1-y}Sb_y$, or $InP_{1-y-z}As_ySb_z$ NCs with $Ga[GaI_4]$ to prepare $In_{1-x}Ga_xAs_{1-y}Sb_y$ ($x = 0$ to 0.83, $y = 0.67$), $In_{1-x}Ga_xP_{1-y}As_y$ ($x = 0$ to 0.7, $y = 0.72$ to 0.83), $In_{1-x}Ga_xP_{1-y}Sb_y$ ($x = 0$ to 0.8, $y = 0.87$), and $In_{1-x}Ga_xP_{1-y-z}As_ySb_z$ ($x = 0$ to 0.9, $y = 0.42$, $z = 0.41$) (Fig. 1E and figs. S8 to S10). The reducing environment provided by $Ga[GaI_4]$ prevented the leaching of the more reactive pnictide so that the initial pnictide-to-pnictide ratios remained unchanged, whereas the Ga:In ratio could be varied precisely (figs. S8 to S10). Raman spectra of quaternary solid-solution NCs showed well-defined peaks, which indicate high crystal quality, and gradual shifts of the phonon mode energies as the composition was tuned, which were consistent with formation of solid solution III-V NCs (fig. S11) (*37*), further corroborated with extensive scanning transmission electron microscopy (STEM)–energy-dispersive x-ray spectroscopy (EDS) and aberration corrected high-resolution STEM (HR-STEM) and HR-TEM studies (figs. S12 to S15).

To test the photophysical properties of quaternary $In_{1-x}Ga_xP_{0.28}As_{0.72}$ NCs ($x = 0$ to 0.7) synthesized in reduced $Ga[GaI_4]$ molten salt, we grew thin wide-bandgap ZnSe shells to passivate

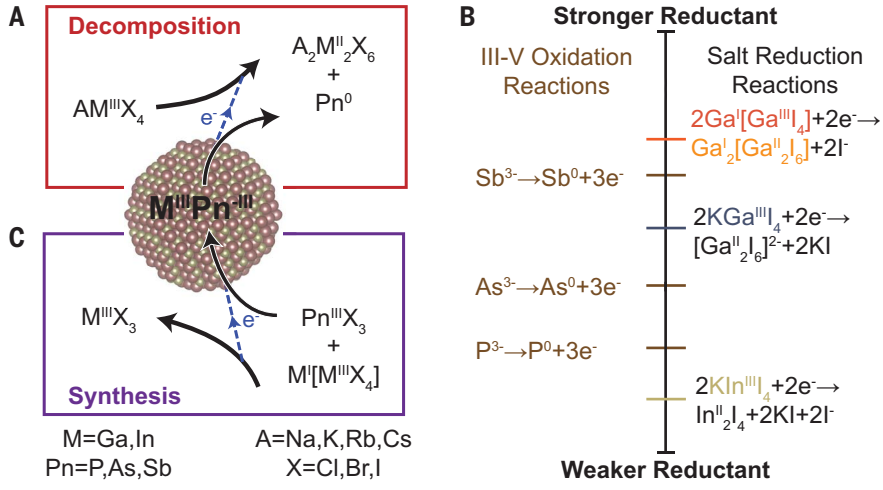

Fig. 2. Molten salt redox chemistry. (**A**) The relation between molten salt redox chemistry and III-V NCs that controls the NCs' chemical stability. (**B**) Qualitative electrochemical scale for key reactions governing the stability of the pnictide component of the III-V NCs compared with redox reactions of III-halide molten salt. (**C**) Molten salt redox chemistry for precursor activation during NC synthesis.

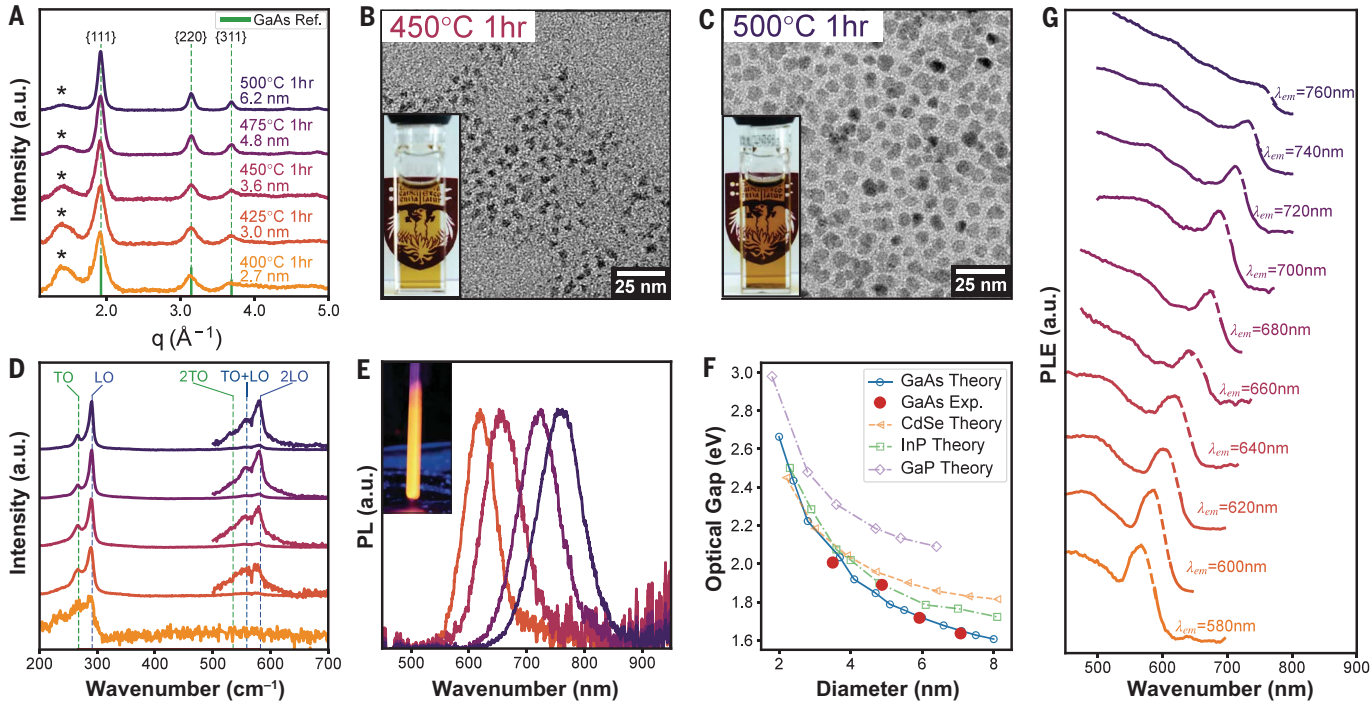

Fig. 3. Direct synthesis of GaAs NCs in molten salt solvents. (**A**) Powder XRD patterns of colloidal GaAs NCs synthesized from $Ga[GaI_4]$ and AsI_3 in molten CsI/NaI/KI eutectic at temperatures from 425° to 500°C. The sample synthesized at 400°C was prepared by using a $KGaI_4$ solvent. The peaks indicated with asterisks originate from x-ray scattering from the organic ligand shell. (**B** and **C**) TEM images of colloidal GaAs NCs synthesized at (B) 450°C and (C) 500°C. (Insets) Photos of the same samples as colloidal solutions in toluene. (**D**) Raman spectra of colloidal GaAs NCs with reference GaAs Raman modes indicated as dotted lines. (**E**) Room-temperature PL from GaAs NCs synthesized at 425° to 500°C. (Inset) Photo of GaAs NCs synthesized at 425°C under ultraviolet illumination. (**F**) Calculated size-dependent optical gap and PL peak position for GaAs NCs compared with those of InP, GaP, and CdSe. Exp., experiment. (**G**) Room-temperature PLE spectra recorded at different emission wavelengths for GaAs NCs.

NC surface states (fig. S16). After this procedure, all samples showed strong near-infrared PL (fig. S16), which demonstrated the viability of molten salt transformation for the preparation of high-quality quaternary III-V semiconductors. The PL efficiency increased with higher temperature and longer annealing time in the molten salts (fig. S17). We observed up to a 70-fold increase in PL efficiency, demonstrating that molten salt processing can greatly enhance the optical properties of colloidal NCs. The ability to independently control the composition of both the metal and pnictide components enabled independent control over the bandgap, lattice parameter, size, and absolute band energies of a III-V material, which have proven instrumental for designing advanced optoelectronic devices grown with MBE and CVD methods.

The critical parameter that controlled redox stability of III-V phases against decomposition

in a molten salt (Fig. 2A) was the relative positions of the redox potentials for the pnictide oxidation and gallium or indium halide reduction. From the Raman studies, we inferred a qualitative order of the electrochemical potentials relevant to the redox chemistry of InP, InAs, and InSb in molten $KGaI_4$ (Fig. 2B). The key takeaway is that the antimonide in InSb was a sufficiently strong reducing agent to reduce Ga^{III} in $KGa^{III}I_4$ to Ga^{II} in the form of $[Ga^{II}_2I_6]^{2-}$ ions, which also explained the instability of group III–antimonide NCs in molten salts. From this result, it is also implied that InSb was not a sufficiently strong reducing agent to further reduce $Ga[GaI_4]$ molten salt to $Ga^{I}_2[Ga^{II}_2I_6]$ (often referred to as "Ga_2I_3") (supplementary text 1). By contrast, As^{-III} in InAs and P^{-III} in InP were not sufficiently strong reducing agents to react with $KGaI_4$, and we did not observe the formation of $[Ga^{II}_2I_6]^{2-}$ ions after reaction with $KGaI_4$ (Fig. 2C and fig. S4). In support of the role of redox potential in controlling the stability of III-V NCs, we found that $KInI_4$ caused oxidative decomposition of InP, InAs, and InSb, which was consistent with the easier reduction of In^{III} to In^{II} or In^{I} as compared with Ga^{III} to Ga^{II} (fig. S18). Altogether, these results demonstrate that the redox potential of the molten salt controls the chemical stability of III-V phases.

Direct synthesis of GaAs NCs in molten salt solvent

Understanding of the role of redox chemistry in molten salts could be applied not only to prevent decomposition of III-V NCs but also to directly synthesize colloidal semiconductors in molten salts, as outlined in the scheme in Fig. 2C. A reduced group III-halide (such as $Ga[GaI_4]$) could serve as a reducing agent for an oxidized pnictide source [such as arsenic triiodide (AsI_3)] to convert it into the reduced Pn^{-III} state (Fig. 2C) and enable formation of a III-V semiconductor phase. For example, we found that $Ga[GaI_4]$ could simultaneously be a reducing agent and a gallium source to activate arsenic halides and prepare GaAs according to the reaction $3Ga[GaI_4](l) + AsI_3(l) \rightarrow GaAs(c) + 5GaI_3(l)$. Given that GaAs is electrochemically stable in $Ga[GaI_4]$, $Ga[GaI_4]$ should have sufficient reducing potential (Fig. 2B) to convert As^{III} to As^{-III}. As a molten salt solvent, $KGaI_4$ with a melting point of 230°C or cesium iodide (CsI)/sodium iodide (NaI)/KI eutectic (melting point 412°C) could be used and provide comparable results (fig. S19).

After the above reaction proceeded for 1 hour at 400° to 500°C [for temperature (T) <425°C, we used only $KGaI_4$], it was cooled to room temperature, and the salt matrix was dissolved in an appropriate polar aprotic solvent, such as *N*,*N*-dimethylformamide (DMF). Synthesized NCs were recovered as a powder, and oleylamine/zinc chloride ligands were installed on the NC surface to enable colloidal dispersion in toluene or other nonpolar solvents [supplementary materials (SM), materials and methods]. Powder XRD patterns (Fig. 3A) show phase-pure zinc blende GaAs with decreasing diffraction peak width, and thus increasing crystallite size, for colloidal GaAs synthesized at increasing reaction temperatures. TEM images of the samples synthesized at 450°C (Fig. 3B), 500°C (Fig. 3C), and other reaction temperatures (fig. S20) show well-separated particles. The inset photos in Fig. 3, B and C, show stable colloidal solutions of the NCs in toluene. Further comprehensive characterizations of GaAs colloids by use of various methods [SAXS, dynamic light scattering (DLS), ultraviolet-visible spectroscopy] (figs. S21 and S22) confirmed the presence of sub-10-nm GaAs NCs with reasonably narrow size distribution (~15% standard deviation about the mean diameter) formed from molecular reagents in molten salts. We concluded that colloidal synthesis in molten salts can precisely balance NC nucleation and growth kinetics, just as is the case for colloidal synthesis in conventional organic solvents. The reactions showed 50 to 60% yield of colloidal NCs (fig. S23), could be scaled up to prepare ~60 mg of material (fig. S24), and could be adopted to Schlenk line–like reaction methodologies (figs. S25 and S26).

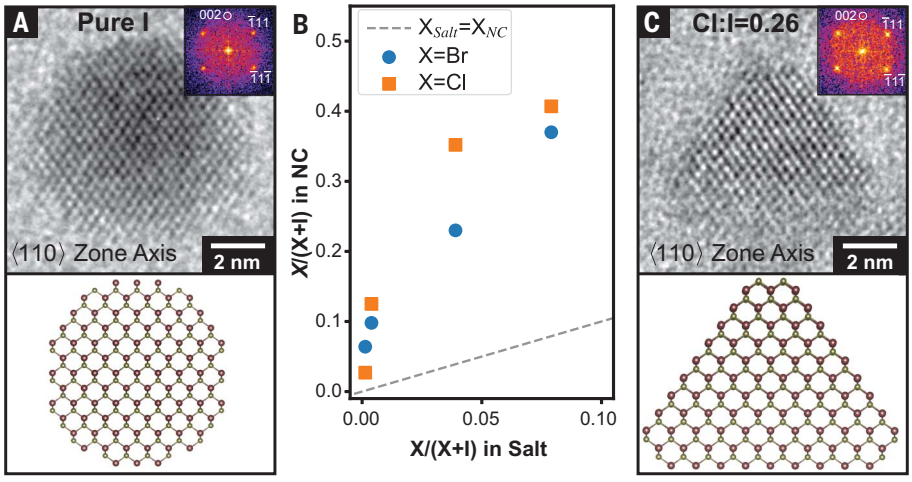

Fig. 4. Salt additives enable shape control. (**A**) HR-TEM image of a GaAs NC viewed down the ⟨110⟩ zone axis synthesized by using CsI/NaI/KI eutectic solvent. (**B**) Plot of the hetero-halide mole fraction added to CsI/NaI/KI molten salt solvent used for GaAs NC growth (*x* axis) versus the hetero-halide mole fraction measured in the recovered NCs (*y* axis). The dashed line indicates a 1:1 correspondence between the solvent and NC halide composition. (**C**) HR-TEM image of a GaAs NC, synthesized by using a Cl:I ratio of 0.26, viewed down the ⟨110⟩ zone axis. In (A) and (C), bottom, are shown atomic models of GaAs viewed down the ⟨110⟩ zone axis with (A) a spherical shape and (C) a tetrahedral shape. (Insets) Fourier transforms of the HR-TEM images.

Raman spectra of GaAs samples synthesized at different temperatures from 400° to 500°C (Fig. 3D and fig. S27) showed a marked trend. For reaction temperatures >425°C, we observed strong GaAs longitudinal optical (LO) and transverse optical (TO) phonon modes as well as overtone peaks, which are an indicator of high crystal quality. By contrast, with temperatures <425°C (and irrespective of solvent used) (fig. S27), we observed poorly defined Raman features, which suggests that the lower reaction temperatures result in low-quality crystals that likely contain vacancy and antisite defects typical for GaAs grown at low temperatures by means of MBE (*24*, *25*) or through colloidal synthesis in organic solvents (*38*). In support of the improvement in crystal quality, samples synthesized between 425° and 500°C showed room-temperature PL (Fig. 3E and fig. S28), but samples synthesized at 400°C or lower temperatures did not show any detectable PL at room or low temperature (77 K) (fig. S29). As such, it appears that high-temperature synthesis is required to produce emissive GaAs NCs. As-synthesized samples showed PL emission bands centered at 617 to 759 nm (2.0 to 1.6 eV). To probe the degree of inhomogeneous broadening, we measured photoluminescence excitation (PLE) spectra of as-synthesized colloids at different detection wavelengths (Fig. 3G). The PLE spectra showed well-resolved excitonic features, which indicates that the GaAs NCs had intrinsically narrow PL linewidth and that the size distribution was the main contributor to the width of the ensemble PL spectra.

We compared the emission photon energy of GaAs NCs to size-dependent optical bandgaps calculated by using atomistic semiempirical pseudopotential methods (*33*, *39*–*41*) combined with the Bethe-Salpeter equation (figs. S30 to S32 and materials and methods) (*42*, *43*). An

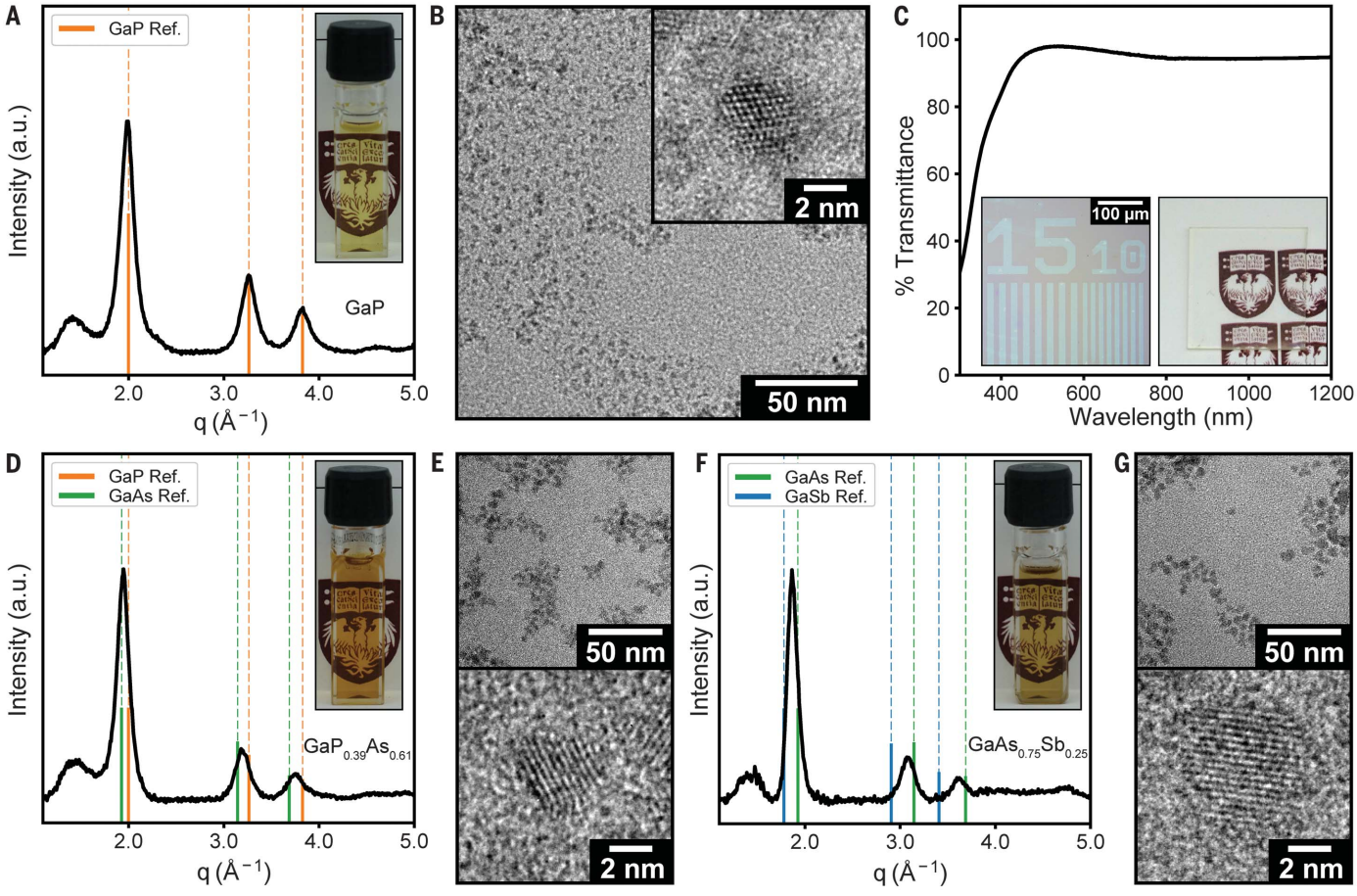

Fig. 5. Expanding the chemical versatility of molten salt media for synthesis of III-V colloidal NCs. (**A**) Powder XRD pattern of GaP NCs. (Inset) Photo of a colloidal solution in toluene. (**B**) TEM and HR-TEM images of GaP NCs. (**C**) Transmittance of a film of GaP NCs deposited on glass substrates. (Insets) (Right) Photo of the sample and (left) optical micrograph of GaP NCs patterned by use of DOLFIN chemistry. (**D**) Powder XRD of $GaP_{1-x}As_x$ NCs. (Inset) Photo of a colloidal solution in toluene. (**E**) TEM and HR-TEM images of $GaP_{1-x}As_x$ NCs. (**F**) Powder XRD of $GaAs_{1-x}Sb_x$ NCs. (Inset) Photo of a colloidal solution in toluene. (**G**) TEM and HR-TEM images of $GaAs_{1-x}Sb_x$ NCs.

excellent agreement between theory and experiment (Fig. 3F) further corroborated our conclusion that the synthesized GaAs NCs are emitting from a band-edge state. The progressive shift of the PLE spectra for different detection wavelengths (Fig. 3G), small Stokes shifts (fig. S33), and nanosecond PL decay lifetimes (figs. S34 and S35) were consistent with band-edge emission. Last, the samples show photoinduced transient-absorption bleach signatures that have strong correspondence with the linear absorption onset, further demonstrating that band-edge carrier dynamics dominated the PL of these materials (figs. S36 to S39). Altogether, our results demonstrate the first example of bright band-edge emission in colloidal GaAs NCs.

The key breakthrough for GaAs NCs is colloidal synthesis at temperatures higher than 425°C, which explains the failure of previous attempts to synthesize GaAs NCs in organic solvents. The need for high-temperature synthesis is related to the rigidity of covalent Ga–As bonds. At the same time, the bond rigidity gives rise to a weak electron-phonon coupling, which is key to the outstanding performance of GaAs in electronic and optoelectronic devices. To demonstrate this point, our calculations show that GaAs NCs have substantially smaller exciton-phonon coupling than cadmium selenide (CdSe) and InP quantum dots (fig. S40), which initial experiments corroborate (figs. S33 and S40).

A HR-TEM image of a GaAs NC synthesized in the CsI/NaI/KI eutectic solvent salt viewed down the ⟨110⟩ zone axis showed a nearly spherical morphology (Fig. 4A and figs. S41 and S42) that is consistent with a Wulff construction with similar surface energy for facets with different Miller indices. In conventional colloidal synthesis (*44*), the addition of surfactants can be instrumental for precise size and shape control of colloidal NCs in molten salts. A surfactant, by definition, should preferentially segregate to an interface and modify the interface energy (*45*). To probe this effect in molten salts, we dosed small amounts of heterohalides (F^-, Cl^-, and Br^-) into the iodide eutectic used for the synthesis of GaAs described above. In Fig. 4B, we plot the added halide ratio in the reaction mixture versus the measured halide ratio in colloidal GaAs NCs. We found nearly fivefold enrichment of Cl^- or Br^- in the recovered NCs, which indicated a preferential binding of Cl^- and Br^- to the surfaces of GaAs NCs. Hard Lewis basic halides such as Cl^- are known to bond more strongly to hard Lewis acids such as Ga^{III} compared with softer halides such as I^- (Ga–I bond dissociation energy, 339 kJ/mol; Ga-Cl bond dissociation energy, 481 kJ/mol) (*46*). The segregation to an interface shows that harder halides demonstrate one characteristic of a surfactant, that of preferential surface binding.

GaAs NCs synthesized with a Cl:I molar ratio of 0.26 commonly showed triangular projections when viewed down the ⟨110⟩ zone axis (Fig. 4C and fig. S43), which was consistent with a tetrahedron shape truncated by

four {111}-type facets. Imaging down the other zone axes (fig. S44) provided further evidence for this morphology. This shape is consistent with the Wulff construction for a crystal, in which the {111} surface energy is much lower than other surfaces, which indicates that Cl^- ions modified the interface energy of GaAs in the molten alkali halide salts. These shape changes were consistent across dozens of particles viewed by TEM and HR-TEM (figs. S41 to S43) and were observed for other halides (F^-) added (fig. S45). The observed shape changes show that chloride ions demonstrate a second characteristic of surfactants, that of modification of the interface energy.

Direct synthesis of other III-V semiconductors in molten salts

The scope of the molten salt redox synthesis of III-V NCs can be extended beyond GaAs. For example, GaP NCs can be accessed through the reaction $3Ga[GaI_4](l) + PI_3(l) \rightarrow GaP(c) + 5GaI_3(l)$. In Fig. 5, A and B, we show an XRD pattern and TEM images of GaP NCs dispersed as colloidal solutions in toluene after oleylamine functionalization confirmed with SAXS (fig. S46). As an indirect-gap semiconductor, GaP should show long excited state lifetimes. Transient absorption studies of our colloidal GaP NCs revealed a 16-ms excited state lifetime (fig. S47); such a long-lived excited state of GaP may be advantageous for use of these NCs for photocatalysis. Furthermore, GaP has a wide bandgap (E_g = 2.24 eV) and high refractive index (n = 3.31 at 633 nm), which is appealing for photonic applications (*47*).

Our computational results (Fig. 3F) show that quantum confinement could further open the bandgap of GaP to as wide as 3 eV for ~2-nm NCs, which would enable a solution-processable material with transparency and high refractive index across the entire visible spectrum. As a proof of concept, we spin-coated films of oleylamine-capped GaP NCs on glass and found excellent transmittance from 450 to 1200 nm (Fig. 5C). Colloidal GaP NCs can be lithographically patterned (SM materials and methods) by using our DOLFIN (direct optical lithography of functional inorganic nanomaterials) photopatterning chemistry (*48*, *49*). The combination of a high refractive index, the low temperatures needed for solution deposition, the ability to mix colloidal NCs with polymers, and direct photolithographic patterning suggests that quantum-confined GaP NCs may enable inexpensive large area patterning of waveguides, metasurfaces, and other photonic elements for visible light.

Mixed-pnictide $GaP_{1-y}As_y$ NCs were directly synthesized from mixtures of AsI_3 and PI_3. A powder XRD pattern consistent with a $GaP_{1-y}As_y$ phase is shown in Fig. 5D, and TEM images (Fig. 5E) showed discrete, well-dispersed colloidal NCs confirmed with SAXS (fig. S48). X-ray fluorescence (XRF) and Raman analysis further supported the formation of solid-solution NCs (figs. S49 and S50). We prepared $GaAs_{1-y}P_y$ NCs for y between 0.03 and 0.75 and thus could tune the bandgap from ~1.7 to 2.4 eV (fig. S51). Last, our reductive chemistry could be expanded to III-Sb materials through the reaction $3Ga[GaI_4](l) + SbI_3(l) \rightarrow GaSb(c) + 5GaI_3(l)$, which results in crystalline GaSb with large (50+ nm) crystallites (figs. S52 and S53). Mixtures of AsI_3 and SbI_3 resulted in $GaAs_{1-y}Sb_y$ NCs (Fig. 5, F and G). These materials showed good crystallinity with TEM and high colloidal stability, and Raman and XRF analyses are consistent with formation of a solid solution (figs. S54 to S56).

Discussion

Our results have demonstrated the versatility of molten salt redox chemistry in the synthesis of colloidal III-V quantum dots. Key concepts from traditional organic solvent–based colloidal chemistry, such as surfactants, were translated to synthesis in molten salt solvents. Drawing connections between molten salts and organic solvents may be helpful in designing future reactions, and further exploration of surfactants in molten salts will expose the full potential of molten salts for precision colloidal synthesis of size-, shape-, and surface termination–controlled nanomaterials.

We have demonstrated nearly a dozen compositions of binary, ternary, quaternary, and pentanary colloidal III-V quantum dots that have thus far not been reported. The combination of cation exchange and direct synthesis of gallium pnictide materials in molten salts presents a rational path to the preparation of III-V quantum dots of nearly any composition and size. Looking forward, the ability to controllably nucleate and grow isolated semiconductor NCs in molten salts at temperatures far above those accessible for organic solvents will likely open a door into synthesis of many previously unknown colloidal nanomaterials.

REFERENCES AND NOTES

1. F. P. García de Arquer *et al*., *Science* **373**, eaaz8541 (2021).
2. C. R. Kagan, L. C. Bassett, C. B. Murray, S. M. Thompson, *Chem. Rev.* **121**, 3186–3233 (2021).
3. D. A. Hanifi *et al*., *Science* **363**, 1199–1202 (2019).
4. Y. Yuan *et al*., *J. Phys. Chem. Lett.* **12**, 7180–7193 (2021).
5. Y. Shirasaki, G. J. Supran, M. G. Bawendi, V. Bulović, *Nat. Photonics* **7**, 13–23 (2013).
6. O. Chen *et al*., *Nat. Mater.* **12**, 445–451 (2013).
7. X. Lan *et al*., *Nat. Mater.* **19**, 323–329 (2020).
8. B. Ji, S. Koley, I. Slobodkin, S. Remennik, U. Banin, *Nano Lett.* **20**, 2387–2395 (2020).
9. M. P. Hendricks, M. P. Campos, G. T. Cleveland, I. Jen-La Plante, J. S. Owen, *Science* **348**, 1226–1230 (2015).
10. Q. A. Akkerman *et al*., *Science* **377**, 1406–1412 (2022).
11. Y.-H. Won *et al*., *Nature* **575**, 634–638 (2019).
12. D. Zhu *et al*., *J. Am. Chem. Soc.* **144**, 10515–10523 (2022).
13. M. Imram *et al*., *Adv. Mater.* **35**, 2306147 (2023).
14. V. Chandrasekaran *et al*., *Nano Lett.* **17**, 6104–6109 (2017).
15. T. Kim *et al*., *Adv. Mater.* **34**, e2110665 (2022).
16. D. C. Gary, B. M. Cossairt, *Chem. Mater.* **25**, 2463–2469 (2013).
17. Q. N. Nguyen, C. Wang, Y. Shang, A. Janssen, Y. Xia, *Chem. Rev.* **123**, 3693–3760 (2023).
18. Z. Ma, J. Mohapatra, K. Wei, J. P. Liu, S. Sun, *Chem. Rev.* **123**, 3904–3943 (2023).
19. S. G. Kwon, T. Hyeon, *Acc. Chem. Res.* **41**, 1696–1709 (2008).
20. J. F. Geisz *et al*., *Nat. Energy* **5**, 326–335 (2020).
21. M. A. Olshavsky, A. N. Goldstein, A. P. Alivisatos, *J. Am. Chem. Soc.* **112**, 9438–9439 (1990).
22. J. Lauth, T. Strupeit, A. Kornowski, H. Weller, *Chem. Mater.* **25**, 1377–1383 (2013).
23. B. J. Beberwyck, A. P. Alivisatos, *J. Am. Chem. Soc.* **134**, 19977–19980 (2012).
24. T. A. Gant, H. Shen, J. R. Flemish, L. Fotiadis, M. Dutta, *Appl. Phys. Lett.* **60**, 1453–1455 (1992).
25. E. S. Harmon *et al*., *Appl. Phys. Lett.* **63**, 2248–2250 (1993).
26. S. K. Gupta, Y. Mao, *J. Phys. Chem. C Nanomater. Interfaces* **125**, 6508–6533 (2021).
27. D. Portehault *et al*., *Chem. Soc. Rev.* **51**, 4828–4866 (2022).
28. H. L. Thi N'Goc *et al*., *Adv. Mater.* **29**, 1604745 (2017).
29. H. Zhang *et al*., *Nature* **542**, 328–331 (2017).
30. V. Kamysbayev *et al*., *ACS Nano* **13**, 5760–5770 (2019).
31. V. Srivastava *et al*., *J. Am. Chem. Soc.* **140**, 12144–12151 (2018).
32. J. C. Ondry, A. Gupta, Z. Zhou, J. H. Chang, D. V. Talapin, *ACS Nano* **18**, 858–873 (2024).
33. A. Gupta *et al*., *J. Am. Chem. Soc.* **145**, 16429–16448 (2023).
34. A. Gupta *et al*., *Nano Lett.* **22**, 6545–6552 (2022).
35. M. H. Hudson, A. Gupta, V. Srivastava, E. M. Janke, D. V. Talapin, *J. Phys. Chem. C Nanomater. Interfaces* **126**, 1564–1580 (2022).
36. N. N. Greenwood, A. Earnshaw, *Chemistry of the Elements* (Elsevier, ed. 2, 1997).
37. P. Mukherjee, S. J. Lim, T. P. Wrobel, R. Bhargava, A. M. Smith, *J. Am. Chem. Soc.* **138**, 10887–10896 (2016).
38. V. Srivastava *et al*., *Nano Lett.* **17**, 2094–2101 (2017).
39. L.-W. Wang, A. Zunger, *Phys. Rev. B Condens. Matter* **51**, 17398–17416 (1995).
40. L.-W. Wang, A. Zunger, *Phys. Rev. B Condens. Matter* **53**, 9579–9582 (1996).
41. E. Rabani, B. Hetényi, B. J. Berne, L. E. Brus, *J. Chem. Phys.* **110**, 5355–5369 (1999).
42. M. Rohlfing, S. G. Louie, *Phys. Rev. B Condens. Matter* **62**, 4927–4944 (2000).
43. H. Eshet, M. Grünwald, E. Rabani, *Nano Lett.* **13**, 5880–5885 (2013).
44. Y. Yin, A. P. Alivisatos, *Nature* **437**, 664–670 (2005).
45. D. H. Everett, *Pure Appl. Chem.* **31**, 577–638 (1972).
46. N. A. Lange, *Lange's Handbook of Chemistry* (McGraw-Hill, ed. 15, 1999).
47. D. J. Wilson *et al*., *Nat. Photonics* **14**, 57–62 (2020).
48. Y. Wang, I. Fedin, H. Zhang, D. V. Talapin, *Science* **357**, 385–388 (2017).
49. J.-A. Pan, H. Cho, I. Coropceanu, H. Wu, D. V. Talapin, *Acc. Chem. Res.* **56**, 2286–2297 (2023).
50. T. Lin, TommyLinkl/III-V-NC_calculations (2024); https://github.com/TommyLinkl/III-V-NC_calculations.

ACKNOWLEDGMENTS

We thank J. Jureller for help in designing apparatus for the high-temperature Raman measurements. We thank the Alivisatos group for use of their spectroscopy equipment and M. Hasham and A. S. Abbas for experimental assistance. We are grateful to A. Nelson for a critical reading and editing of the manuscript. **Funding:** The work on cation exchange reactions in reducing molten salts was supported by the Samsung QD Cluster Collaboration. The work on direct synthesis of III-V quantum dots and high-angle annular dark-field (HAADF)–STEM and STEM-EDS imaging was supported by the National Science Foundation Science and Technology Center (STC) for Integration of Modern Optoelectronic Materials on Demand (IMOD) under award DMR-2019444. Spectroscopic studies were supported by the Department of Defense Air Force Office of Scientific Research under grant FA9550-22-1-0283. Advanced data analysis was supported by MICCoM, as part of the Computational Materials Sciences Program funded by the US Department of Energy, Office of Science, Basic Energy Sciences, Materials Sciences and Engineering Division, under grant DOE/BES 5J-30161-0010A. The theoretical and computational work was supported by the US Department of Energy, Office of Science, Office of Basic Energy Sciences, Materials Sciences and Engineering Division, under contract DE461AC02-05-CH11231 within the Fundamentals of Semiconductor Nanowire Program (KCPY23). This work made use of the shared facilities at the University of Chicago Materials

Research Science and Engineering Center, supported by National Science Foundation under award DMR-2011854. Parts of this work were carried out at the Soft Matter Characterization Facility of the University of Chicago. HAADF-STEM and STEM-EDS imaging were carried out at the Facility for Electron Microscopy of Materials at the University of Colorado at Boulder (CU FEMM, RRID: SCR_019306). A.J. is partially supported by a graduate fellowship from Kwanjeong Educational Foundation. B.F.H. acknowledges support from the National Science Foundation through the Graduate Research Fellowship Program (NSF-GRFP) under grant DGE 2040434. Work performed at the Center for Nanoscale Materials, a US Department of Energy Office of Science User Facility, was supported by the US DOE, Office of Basic Energy Sciences, under contract DE-AC02-06CH11357. **Author contributions:** J.C.O. conceived, designed, and performed cation exchange, direct synthesis, structural characterization, and optical characterization experiments; analyzed data; and cowrote the manuscript. Z.Z. designed and performed GaP and part of $GaAs_{1-y}P_y$ by direct synthesis, patterning experiments, and Raman study of directly synthesized GaAs NCs and supported manuscript writing. K.L. performed all electronic structure calculations, analyzed data, and supported manuscript writing. A.G. and J.H.C. contributed to molten salt development. H.W. performed NC patterning experiments. A.J. performed SAXS and DLS experiments. D.W. supported elemental analysis and x-ray characterization. H.C.F. performed millisecond transient absorption experiments. B.F.H. performed and analyzed aberration-corrected STEM (AC-STEM) and STEM-EDS characterization. S.Y. and G.D. supervised AC-STEM and STEM-EDS characterization, and G.D. acquired funding. R.D.S. provided femtosecond transient absorption spectroscopy and supported data collection and analysis. E.R. supervised electronic structure calculations, acquired funding, and supported manuscript writing. D.V.T. conceived and supervised the project, acquired funding, and cowrote the manuscript. All authors discussed the results and commented on the manuscript. **Competing interests:** J.C.O., Z.Z., and D.V.T. have filed provisional patents (US patent application nos. 63/562,873 and 63/662,511) related to this work. **Data and materials availability:** All data needed to evaluate the conclusions in the paper are present in the paper and the supplementary materials. The samples can be provided by the authors under a materials transfer agreement with the university. The code and data for the theoretical modeling and electronic structure calculations in this work are provided in a public repository (*50*). Correspondence and requests for materials should be addressed to D.V.T. (dvtalapin@uchicago.edu).

SUPPLEMENTARY MATERIALS

science.org/doi/10.1126/science.ado7088
Materials and Methods
Supplementary Notes
Figs. S1 to S56
References (*51–107*)

Submitted 16 February 2024; accepted 6 September 2024
10.1126/science.ado7088